



Effect of shear bond failure on the strength ratio in DEM modeling of quasi-brittle materials

Yifei Ma¹ · Haiying Huang²

Received: 24 October 2020 / Accepted: 2 May 2021 / Published online: 10 June 2021
 © The Author(s), under exclusive licence to Springer-Verlag GmbH Germany, part of Springer Nature 2021

Abstract

Displacement softening has shown to be an effective ingredient to overcome common deficiencies associated with DEM modeling based on bonded spherical particles (Ma and Huang in Int J Rock Mech Min Sci 104:9–19, 2018b). By incorporating a softening path in the normal force–displacement contact law, we show that the softening contact model can not only yield a realistic compressive over tensile strength ratio as high as about 30, but also capture the highly nonlinear failure envelope at the confined extension stress range, typical for quasi-brittle materials such as rocks and concretes. In our previous model, bond breakage at the particle scale is governed by the normal bond strength only. Here, we generalize the model by removing the restriction on the shear bond failure. Formulation of the displacement-softening model is first introduced. Novel features from modeling the behaviors of Berea sandstone without considering shear bond failure are summarized. How material behaviors at both the micro- and macroscale are affected by the inclusion of shear bond failure is then analyzed. Finally, implications of the numerical results in the context of how to calibrate material properties for DEM modeling in general is discussed.

Keywords Discrete element method · Displacement softening contact model · Shear bond failure · Strength ratio

List of symbols

β	Reciprocal of the softening coefficient χ	ω	ratio between the limiting confining stress where the tension cutoff ends and the uniaxial tensile strength
χ	Softening coefficient	$\bar{\delta}_*$	Normal bond stretch when the bond breaks (m)
χ_*	Critical value of χ	$\bar{\delta}_c, \bar{\delta}_2$	Critical stretch (m)
η_{sc}	Percentage of shear micro-cracks at 80% of the post-peak loading level in the uniaxial compression test	$\bar{\delta}_n$	Normal bond stretch (m)
η_{st}	Percentage of shear micro-cracks at 80% of the post-peak loading level in the direct tension test	$\bar{\kappa}$	Area contact (bond) stiffness ratio
η_s	Percentage of shear micro-cracks at the peak stress level	$\bar{\sigma}_c$	Normal bond strength
κ	Normal over shear stiffness ratio of the point contact	$\bar{\tau}_c$	Shear bond strength
μ	Coulomb's friction coefficient	$\bar{\theta}$	relative angle of rotation between the particles
		\bar{E}_c	Area contact (bond) modulus (GPa)
		\bar{F}_{nmax}	Maximum normal bond force (N)
		\bar{F}_n	Normal bond force (N)
		\bar{F}_s	Shear bond force (N)
		\bar{k}_ℓ	Normal bond stiffness of the elastic loading path (N/m)
		\bar{k}_u	Normal bond stiffness of the softening path (N/m)
		\bar{M}^n	Twisting moment (N m)
		\bar{R}	Bond radius (m)
		\bar{U}_b	Nominal energy loss density associated with one bond breakage (MPa)
		σ_1	Maximum principal stress (MPa)

✉ Haiying Huang
 haiying.huang@ce.gatech.edu

¹ Department of Civil and Architectural Engineering, Lawrence Technological University, Southfield, MI 48075, USA

² School of Civil and Environmental Engineering, Georgia Institute of Technology, Atlanta, GA 30332, USA

σ_3	Minimum principal stress (MPa)
σ_c , UCS	Uniaxial compressive strength (MPa)
σ_t , UTS	Uniaxial tensile strength (MPa)
ϖ	Shear over normal bond strength ratio
A	Cross-sectional area of the bond (m^2)
D	Diameter of the cylindrical assembly (mm)
E_c	Point contact modulus (GPa)
H	Height of the cylindrical assembly (mm)
J	Polar moment of inertia (m^4)
N	Total number of micro-cracks at the peak stress

1 Introduction

Failure in many engineering problems involves more than one mechanism. For example, in landslide, shear slip may occur after development of tensile cracks in the crest of a slope [26]; in drilling or mechanical excavation, damage induced right underneath the tool combined with rock chipping and fragmentation contributes to the total volume removal [6]; both breakout and drilling-induced fracturing are possible scenarios associated with borehole instability [7]. Discrete element method (DEM) [4] has a unique advantage over continuum mechanics based numerical methods in modeling this class of problems, where multiple modes of failure may occur. In DEM, both brittle fracture and plastic flow can be modeled simultaneously within the same constitutive framework defined by the contact laws at the microscale. In general, no continuum-scale constitutive model is required as direct input for a DEM model. The obvious drawback is that calibration of the material properties between the micro- and macroscale becomes a prerequisite.

It is natural to ask which macroscale material properties a DEM model need to be calibrated against before it can be considered an adequate representation of a real material. The answer is obviously problem specific. In the literature, the calibration process for quasi-brittle materials such as rocks and concretes is often limited to elastic constants and the uniaxial compressive strength. This could be sufficient if the material of interest is mostly linear elastic prior to reaching the strength and the problem involves only compressive shear failure. However, for the class of problems involving both tensile fracture and plastic shear failure, with the premise that macroscale failure mechanisms can be reproduced by the DEM model, tensile strength or the compressive over tensile strength ratio UCS/UTS, the full failure envelope and the mode I fracture toughness become

the additional elements necessary for the DEM model to be validated against.

UCS/UTS can be viewed as a measure of material brittleness. If the material is in a confined extension stress state, a low UCS/UTS means that the material is more likely to fail in shear at the macroscale, while a high UCS/UTS means that brittle tensile failure is more likely to occur. For example, in the Brazilian tensile test, a low UCS/UTS could result in plastic shear failure near the loading platens with the development of the tensile center crack being suppressed [5, 16]. Diametrical splitting caused by tensile crack growth from the center of the specimen occurs only if the UCS/UTS is relatively high. The strength ratio therefore directly affects the macroscale failure mechanisms and the transition between the ductile and brittle failure modes if both are present in the problem of interest.

For DEM with bonded spherical particles, UCS/UTS $\sim 4\text{--}5$ is about the maximum that a dense bonded particle assembly can attain if the interaction between the spherical particles is limited to short-range, elasto-perfectly brittle and frictional [11, 22]. Moreover, the corresponding failure envelope in the confined extension region is rather linear. In comparison, the strength ratio for rocks and concretes is in the range of 10–30 [9, 10] and the failure envelope generally exhibits highly nonlinear characteristics. This issue of the low strength ratio has been one of the major hurdles for effective DEM application in modeling rock behaviors.

A few numerical strategies, e.g., clumping/clustering particles, increasing the particle interaction range or using multiscale representation of the grain structure and rock fabric, have been suggested in the literature to address the issue of the low strength ratio [3, 19–21, 25]. Nevertheless, DEM modeling with spherical particles having only short-range interactions has its appeal in its computational efficiency. Our recent development of a displacement-softening contact model [17] shows that incorporating displacement softening into the contact law is effective in not only overcoming the issue of low strength ratio, but also accurately capturing the high nonlinearity in the failure envelope of rocks in the confined extension range. Most notably, the DEM model gives an excellent match with the experimental data [1] for the full failure envelope of Berea sandstone up to the confinement around $\sigma_3 \simeq 100$ MPa, beyond which compaction failure is known to take place [29]. However, in this DEM model, bond failure is governed exclusively by the normal bond strength. Failure due to shear bond strength is not considered.

Basic elements in contact laws for bonded particles models usually include elastic components characterized by contact stiffnesses and inelastic components, which are often described by normal and shear bond strengths,

interparticle frictional coefficient, etc. (e.g., [22]). While it is relatively straightforward to determine the contact parameters for the elastic components with dimensional analysis and rule of mixtures serving as the starting point [13, 23], there is ambiguity in the choice of the parameters for the inelastic components, for example, how to determine the ratio between the shear and normal bond strengths. Experimental evidences suggest that even in tests such as hydraulic fracturing in granite, where mode I brittle failure is typically observed at the macroscale, source mechanisms of acoustic emission (AE) events still indicate there are small percentages of shear and mixed modes events [8]. Though the AE source mechanisms, which characterize the deformation modes of the microscale failure events, do not equate to the bond failure mechanisms dictated by the bond strengths in DEM modeling, it is reasonable to ask how the shear bond failure affects the micro- and macroscale material behaviors within the framework of the displacement-softening contact model.

The present study is a continuation of our numerical development in Ma and Huang [17] in search of contact laws for bonded spherical particles to realistically model rock behaviors. The work in Ma and Huang [17] is extended here with the restriction on shear bond failure removed. Effects of the shear bond failure on the strength ratio UCS/UTS and the associated failure mechanisms are examined for the linear softening contact model. The reason we focus on UCS/UTS is because for a finely discretized particle assembly, the strengths can be made mostly particle size independent and scale linearly with respect to the bond strengths [15, 17]. Since fracture toughness of a particle assembly can be considered a function of the tensile strength and the particle size, once the strengths of a DEM model are properly calibrated, fracture toughness can be adjusted through the particle size. For these reasons, UCS/UTS is the most critical aspect in the material properties calibration process for DEM modeling. In this work, we limit the scope to the case when the normal bond component follows the linear softening law and the shear bond component remains elasto-perfectly brittle, however, with the shear bond strength being such that both normal and shear bond failures are possible. Consequently, the strength ratio UCS/UTS is now primarily affected by both the shear over normal bond strength ratio and the softening coefficient in the contact model.

Formulation of the contact model is first introduced. Numerical results from modeling Berea sandstone without considering shear bond failure are summarized. Numerical simulations are then conducted to investigate the effects of the shear over normal bond strength ratio as well as the softening coefficient on the uniaxial compressive and tensile strengths and the corresponding micro- and macroscale

failure mechanisms. Finally, implications of the numerical results in the context of how to choose contact parameters for constructing a high-fidelity DEM model for materials such as rocks are discussed.

2 Contact model formulation

The displacement-softening model is developed by modifying the parallel bond model in the DEM code *PFC 5* [14]. The original parallel bond model has two contact components, a particle–particle point contact and an area contact through the bond in between the particles. The contact forces are superimposed from the two components. Bending and twisting moments can be transmitted through the area contact. The point contact is elastic and frictional, while the area contact is elasto-perfectly brittle. The normal and shear stiffnesses for the contact components are prescribed through the contact moduli and the stiffness ratios. The input parameters for the point contact include, point contact modulus E_c , the normal over shear stiffness ratio κ and Coulomb's friction coefficient μ . Similarly, the elastic force–displacement relationships for the area contact are described through the area contact modulus \bar{E}_c and the stiffness ratio $\bar{\kappa}$. Detailed formulation of the parallel bond model can be found in Potyondy and Cundall [22].

In the displacement-softening contact model [17], a linear softening path is incorporated in the force–displacement law in the normal bond component, see Fig. 1. Here, compression and stretch of the bond are taken as positive. For a bond in stretch, onset of softening occurs if the normal bond force reaches its maximum, $\bar{F}_{n\max} = -\bar{\sigma}_c A$, where $\bar{\sigma}_c$ is the normal bond strength and $A = \pi\bar{R}^2$ is the cross-sectional area of the bond of radius \bar{R} . The softening path is defined by the softening coefficient χ ,

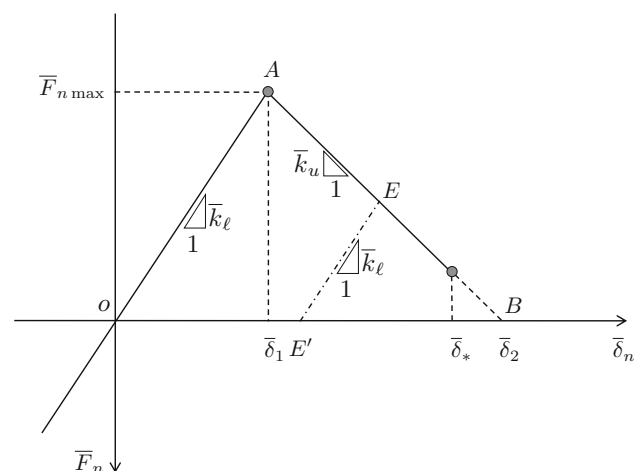


Fig. 1 Force–displacement contact law for the normal bond

a ratio between the normal stiffnesses along the elastic loading and softening paths, $\chi = \bar{k}_\ell / \bar{k}_u$. The perfectly brittle parallel bond model is recovered if $\chi = 0$. If χ is large, it means that the normal bond contact is nearly elasto-perfectly plastic.

The bond fails if one of the criteria below is met at the contact,

$$\bar{\delta}_n + \bar{R}|\bar{\theta}| \geq \bar{\delta}_c \tag{1}$$

$$\frac{|\bar{F}_s|}{A} + \frac{|\bar{M}^n| \bar{R}}{J} \geq \bar{\tau}_c \tag{2}$$

where \bar{F}_s is the shear bond force; $|\bar{M}^n|$ is the twisting moment; J is the polar moment of inertia; $\bar{\delta}_n$ is the normal bond stretch; $\bar{\theta}$ is the relative angle of rotation between the particles; $\bar{\tau}_c$ is the shear bond strength; and $\bar{\delta}_c$ is the critical stretch defined according to,

$$\bar{\delta}_c \equiv \bar{\delta}_2 = \frac{\bar{\sigma}_c A}{\bar{k}_\ell} (1 + \chi) \tag{3}$$

If we make an analogy between the bond and a beam cross section, the failure criterion for the normal component, Eq. 1, is essentially equivalent to state that a bond breaks when the stretch at the outer edge of the bond reaches a critical value. In other words, $\bar{\delta}_n$ is the stretch on the neutral plane of the bond; when the normal bond breaks, $\bar{\delta}_n = \bar{\delta}_* = \bar{\delta}_c - \bar{R}|\bar{\theta}|$. Once a failure condition is reached, both the normal and shear contact forces in the bond are immediately reduced to zero and the contact is active only through the point contact component. Bond breakage is termed here a micro-crack event, tensile according to Eq. 1 and shear according to Eq. 2. The contact model formulated above is implemented as a user-defined model in PFC 5.

When shear bond failure is not considered, the failure mechanism is tension-governed. The uniaxial strengths are affected by not only the normal bond strength $\bar{\sigma}_c$, but also the nominal energy loss density \bar{U}_b associated with one bond breakage,

$$\bar{U}_b = (1 + \chi) \frac{\bar{\sigma}_c^2}{\bar{E}_c} \tag{4}$$

If $\bar{\sigma}_c$ remains constant, \bar{U}_b increases with χ . Consequently, the uniaxial strength is expected to increase with χ . However, as shown in our previous work [17], when χ is smaller than a threshold value, $\chi \lesssim 0.286$ or $1/\chi \geq 3.5$ for 2D simulations with the parameter set in Ma and Huang [17], the soften coefficient χ has little effect on both UTS and UCS and the strength ratio remains nearly constant, $UCS/UTS \simeq 3.7$, see Fig. 2. This could be explained by the fact that when a bond softens, the unloading process is controlled by the softer one between the bond and the local

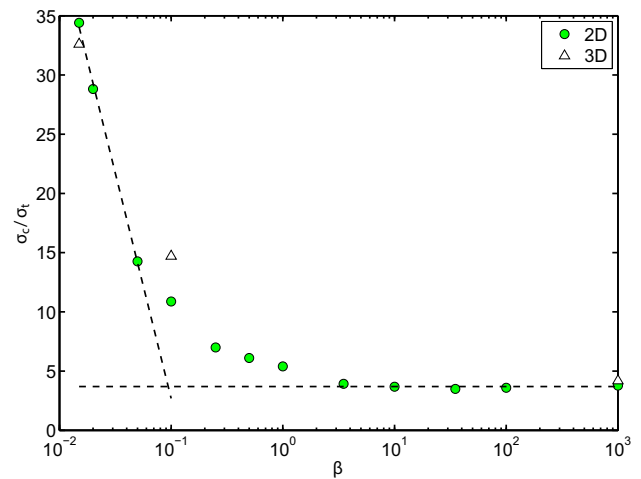


Fig. 2 Variation of the strength ratio with the reciprocal of the softening coefficient, $\beta = 1/\chi$ [17]

domain outside of the bond. When χ is small, softening at a contact is basically dominated by the outside domain, not the softening bond itself, which makes the unloading behavior effectively the same as that of a perfectly brittle model. Meanwhile, when $\chi \gtrsim 0.286$, the strength ratio increases with χ . The trend from the 2D simulations can be fit according to,

$$UCS/UTS = -35.3626 - 16.5274 \ln \beta \tag{5}$$

where β is the reciprocal of the softening coefficient, $\beta = 1/\chi$. At $\beta = 0.015$ ($\chi = 66.67$), $UCS/UTS = 35.35$ is about the upper limit for most rocks.

Compared with the original parallel bond model, the softening coefficient χ is the only additional parameter introduced in the contact model. It follows from dimensional analysis that for a given particle assembly, after the elastic properties are determined, the nature of bond failure is controlled by $\bar{\sigma}_c$, $\bar{\tau}_c$ and χ or in the dimensionless form, ϖ and χ , where $\varpi = \bar{\tau}_c / \bar{\sigma}_c$ is the shear over normal bond strength ratio. Our analysis next therefore focuses on the effects of the bond strength ratio ϖ and the softening coefficient χ on UCS/UTS and the failure behaviors of a particle assembly through numerical simulations of unconfined tests. We limit the range of χ to $0.286 < \chi \leq 100$ with the case of $\chi = 0$ serving as a reference.

3 Modeling of Berea sandstone

We start first with a baseline case where the microscale parameters yield macroscale properties similar to those of Berea sandstone reported in the literature [1, 28, 30]. A cylindrical sample of diameter $D = 40$ mm and height $H = 80$ mm is employed for the compression and direct tension tests. The particle assembly is randomly generated with

particle radii following a uniform distribution, $\bar{R} = 0.8\text{--}1.66$ mm, and density $\rho = 2630\text{ kg/m}^3$. The total number of particles in the domain is about 13,000. The compression test is modeled with the boundary conditions applied through rigid wall elements, while direct tension is simulated by applying the velocity to the layers of particles that are gripped together at the top and bottom of the sample. To eliminate the lateral confinement near the loading surfaces, frictionless ball–wall contact is applied to the compression test and only axial movement of the gripped particles is restrained in direct tension. The contact parameters for the baseline case are listed in Table 1. Both the shear and normal bond strengths follow Gaussian distributions. Here, the shear bond strength $\bar{\tau}_c$ is set to be more than 20 times the normal bond strength $\bar{\sigma}_c$. At the microscale, the bonds all break according to the normal failure condition in Eq. 1.

We choose this set of contact parameters by first determining the stiffnesses from the elastic constants. The softening coefficient χ is determined next based on UCS/UTS of Berea sandstone with Eq. 5 and Fig. 2, though mostly from 2D simulations, serving as our guide. Finally, the mean normal bond strength $\bar{\sigma}_c$ is set based on the proportionality between the strengths at the macro- and microscale, i.e., $\text{UCS} \propto \bar{\sigma}_c$.

The complete stress–strain curves from the uniaxial compression and direct tension simulations are shown in Fig. 3. Due to scarcity of the stress–strain curves for direct tension in the literature, only the curve from uniaxial compression is compared with the data from a laboratory experiment [27]. The numerical result misses the nonlinear portion at small strain, which can be attributed to closure of the space between the specimen and the loading platen in the experiment as well as closure of pre-existing micro-cracks and flaws. Apart from that, the two stress–strain curves for uniaxial compression are in reasonable agreement. Young’s modulus and the peak stress are $E \simeq 17.27\text{ GPa}$ and $\sigma_c \simeq 87.16\text{ MPa}$ from the simulation and

Table 1 Microscale contact parameters for the Berea sandstone model

Parameter	Value
Particle contact modulus E_c (GPa)	20
Particle stiffness ratio $\kappa = k_n/k_s$	4.0
Friction coefficient μ	0.5
Bond modulus \bar{E}_c (GPa)	20
Bond stiffness ratio $\bar{\kappa} = \bar{k}_n/\bar{k}_s$	4.0
Shear bond strength $\bar{\tau}_c$ (MPa)	320 ± 32
Normal bond strength $\bar{\sigma}_c$ (MPa)	15 ± 1.5
Softening coefficient χ	6.67

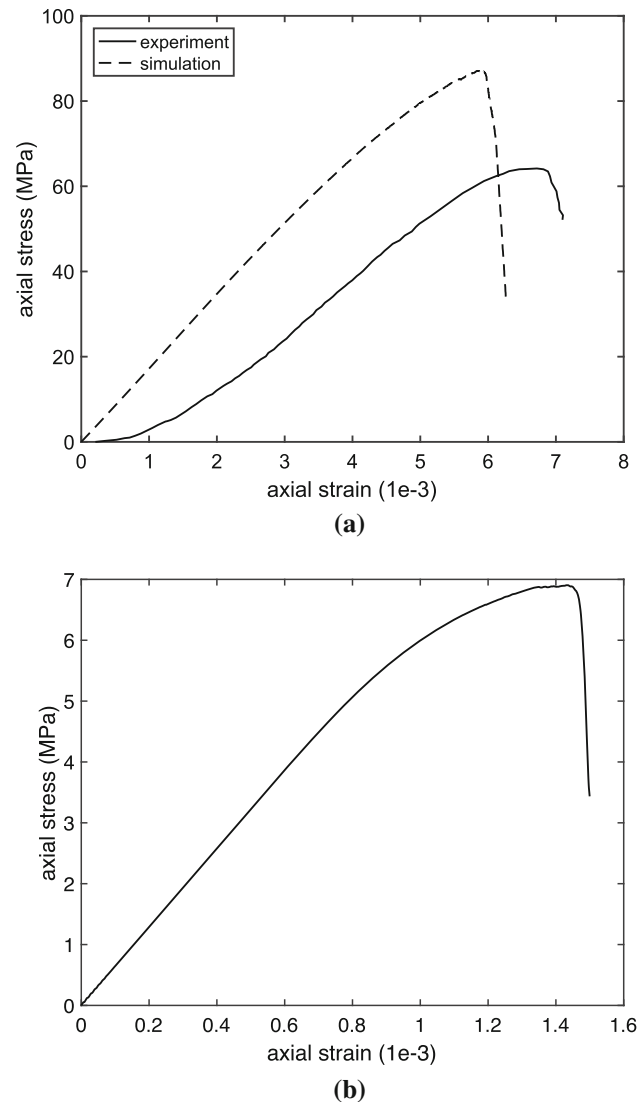


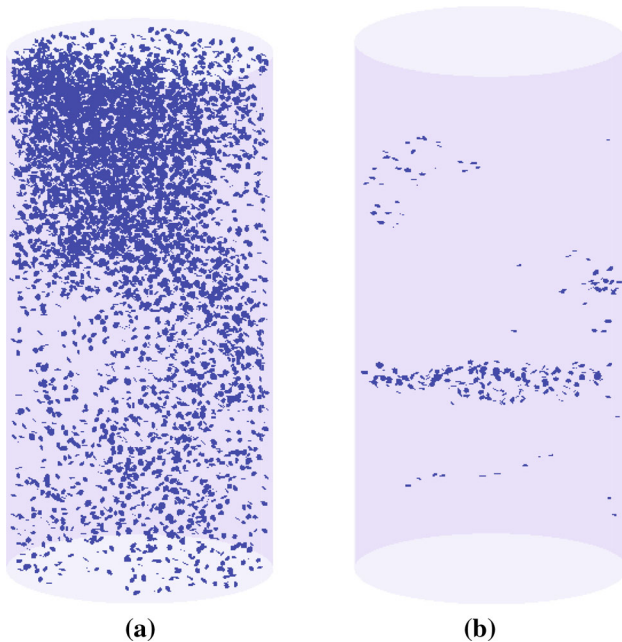
Fig. 3 Stress–strain curves from the baseline simulations with $\chi = 6.67$; **a** uniaxial compression, experimental data digitized from Tarokh and Fakhimi [27], **b** direct tension

$E \simeq 13.96\text{ GPa}$ and $\sigma_c \simeq 65\text{ MPa}$ from the experiment. Overall, the mechanical properties between the numerical simulations and experimental results [1, 27, 28, 30] are in good agreement, see Table 2. Strength ratio of the numerical model, $\sigma_c/\sigma_t = 12.63$, is about the mean of the range of 10–16 from laboratory experiments [1].

The corresponding failure mechanisms from the numerical simulations are shown in Fig. 4. Though the micro-cracks all result from bond failure in tension, coalescence of micro-cracks yields macroscale failure patterns which can be interpreted as shear localization in the compression test and a very well defined mode I tensile crack in direct tension. Here, a micro-crack corresponds to a broken bond and is represented by a circle perpendicular to its contact axis. In general, the macroscale failure

Table 2 Comparison of the mechanical properties between numerical simulations and experimental results from Berea sandstone

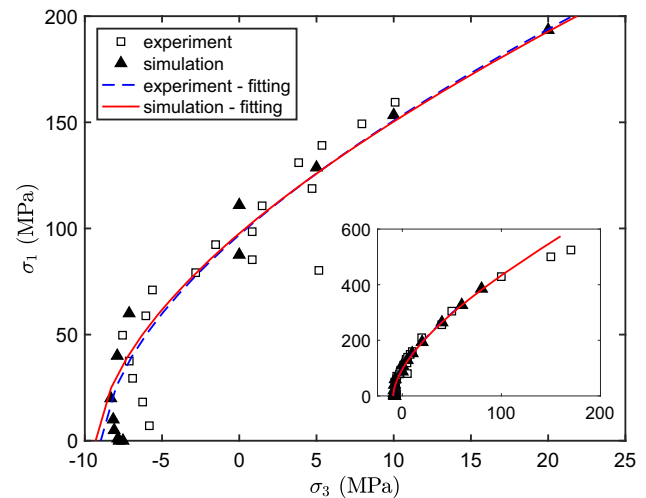
	Simulation	Experiment			
		Bobich [1]	Tarokh and Fakhimi [27]	Zietlow and Labuz [30]	Teufel and Clark [28]
σ_c (MPa)	87.16	79	65	55–65	80
σ_t (MPa)	6.90	4.9–7.3		8.6 (bending)	4.9 ± 0.2
σ_c/σ_t	12.63	10–16			
E (GPa)	17.27		13.96	14	24
ν	0.3			0.32	0.28

**Fig. 4** Distributions of micro-cracks from the baseline simulations at 80% of the post-peak loading level; **a** uniaxial compression, **b** direct tension; blue for tensile micro-cracks

mechanisms from the numerical simulations are similar to the observations from laboratory experiments [1].

Failure envelope obtained from the numerical triaxial extension and compression tests in Ma and Huang [16] is compared with those from the experiments on Berea sandstone in Bobich [1]. As shown in Fig. 5, the full failure envelope from the experiments is very well captured by the numerical simulations up to a confinement about $\sigma_3 \simeq 100$ MPa. The fitting functions in form of Hoek–Brown criteria are nearly identical between the two. The discrepancy at $\sigma_3 \gtrsim 100$ MPa is likely due to the fact that Berea sandstone undergoes shear enhanced compaction [29], a failure mechanism not considered in this DEM model.

The most surprising aspect of this comparison is that the numerical simulations seem to agree with the experimental observations that in the confined extension range, the

**Fig. 5** Comparison of the failure envelopes between the simulations and the experiments of Berea sandstone [1]; fitted by Hoek–Brown criteria

failure envelope may be approximated by a maximum tensile strength criterion if the magnitude of the confining stress is below a threshold, $\sigma_1 \lesssim 60$ MPa in this case. To the best of our knowledge, this is the first numerical evidence suggesting that the use of a tension cutoff in combination with a shear failure criteria for continuum mechanics based numerical modeling is justified.

Experimental research on rock behaviors under confined tension has been scarce. The seminal work by Brace [2] is the primary source that provided experimental support for using a tension cutoff. Out of twenty triaxial extension tests conducted with dog-bone shaped specimens of five rock types, i.e., granite, quartzite, diabase and two dolomites, seven samples fail at axial stresses close to their uniaxial tensile strengths and with the failure planes more or less normal to the axial direction. The experimental work by Ramsey and Chester [24] with Carrara marble also seems to affirm the legitimacy of a tension cutoff.

Both the simulations and experiments show that the compressive strength is somewhat affected by the test configuration, as expected. At $\sigma_3 \simeq 0$, out of the three

experimental data points in Fig. 5, the smallest one is from triaxial compression while the larger two are from triaxial extension. Between the two numerical data points, the larger one, $\sigma_c = 108.35$ MPa, is obtained from the triaxial compression setup with the lateral servo-controlled wall subjected to a very small nominal confining stress, whereas the smaller one is obtained from the uniaxial test setup with the lateral wall removed.

4 Effect of the bond strength ratio

Though we have modeled Berea sandstone successfully, from the point of view of contact model development, it is necessary to address the question of how the material behaviors are affected if the shear bond failure is considered within the context of the displacement softening model. We therefore perform a series of numerical simulations to analyze the effect of shear bond failure by varying the shear bond strength $\bar{\tau}_c$ while keeping the normal bond strength $\bar{\sigma}_c$ and the softening coefficient χ constant. As mentioned earlier, the nature of bond failure is governed by two dimensionless parameters: $\varpi = \bar{\tau}_c/\bar{\sigma}_c$ and χ . In addition to the softening coefficient $\chi = 6.67$ used in the Berea sandstone model, two sets of simulations with $\chi = 0$ and 2 are conducted for comparison purposes. $\chi = 0$ is the perfectly brittle contact case. In each set, the shear bond strength $\bar{\tau}_c$ decreases from 320 ± 32 to 5 ± 0.5 MPa. This corresponds to a range of the mean bond strength ratio $\varpi = 21.33 \sim 0.33$. The Berea sandstone model corresponds to $\varpi = 21.33$ and $\chi = 6.67$. For each combination of χ and ϖ , uniaxial compression and direct tension tests are performed to obtain the uniaxial strengths and the corresponding strength ratio UCS/UTS. All other parameters remain the same as those listed in Table 1.

Dependence of UCS/UTS on the bond strength ratio ϖ is shown in Fig. 6. For a given softening coefficient χ , UCS/UTS first increases nearly linearly when the bond strength ratio ϖ is relatively small, but then reaches a plateau as ϖ becomes large. The plateaus, UCS/UTS = 5.07, 8.95, 12.63, are reached at $\varpi = 2, 6.67, 10$ for $\chi = 0, 2, 6.67$, respectively. It can be seen that when $\varpi \lesssim 1$ or $\bar{\tau}_c \lesssim \bar{\sigma}_c$, UCS/UTS is independent of χ . This means when $\bar{\tau}_c \lesssim \bar{\sigma}_c$, bond breakage is mostly controlled by $\bar{\tau}_c$. Therefore, the softening law in the normal component is ineffective. On the other hand, when ϖ is large, i.e., $\bar{\tau}_c \gg \bar{\sigma}_c$, failure of the bonds is governed by the softening law. Consequently, increase in the softening coefficient χ alone is effective in raising the upper limit of UCS/UTS for a given set of parameters.

Dependence of UCS/UTS on ϖ could also be analyzed from the perspective of the shear and tensile micro-crack percentages in the uniaxial tests. Denote η_{sc} and η_{st} as the

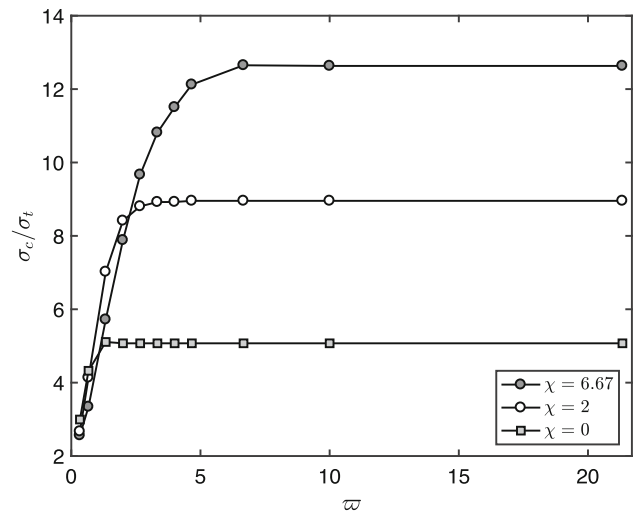


Fig. 6 Compressive over tensile strength ratio UCS/UTS as a function of the bond strength ratio ϖ for $\chi = 0, 2$ and 6.67

percentages of shear micro-cracks measured at 80% of the post-peak loading level in the uniaxial compression and direct tension test, respectively. Subscript c refers to compression and t tension. Percentages of the tensile micro-cracks in the uniaxial tests are therefore $100\% - \eta_{sc}$ and $100\% - \eta_{st}$. If the micro-cracks are all of tensile origin, $\eta_{sc} = \eta_{st} = 0$. The choice of the 80% post-peak loading level is arbitrary, but is based on the observation that at this loading level, the macroscale failure patterns are well developed. In the present work, all the results pertaining to the micro-cracks are obtained at this loading level.

Variations of η_{sc} and η_{st} with ϖ for $\chi = 0, 2$ and 6.67 are shown in Fig. 7. Only shear micro-cracks are present when the bond strength ratio ϖ is relatively small. As ϖ increases, the percentage of shear cracks decreases in both

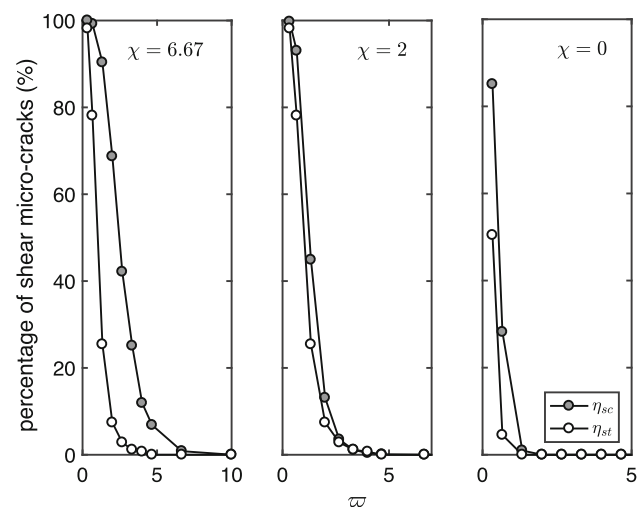


Fig. 7 Variations of the shear micro-crack percentage with the bond strength ratio ϖ at 80% of the post-peak loading level from the uniaxial compression and direct tension tests

the compression and tension tests. Both η_{sc} and η_{st} decrease to zero as ϖ is above some threshold values and η_{st} decreases to zero at a smaller ϖ than η_{sc} . For a given χ , the threshold ϖ above which $\eta_{sc} = \eta_{st} = 0$ coincides with the critical value of ϖ where UCS/UTS reaches a plateau, e.g., $\varpi = 10$ for $\chi = 6.67$. This suggests that when ϖ is large, there are only tensile micro-cracks in both the compression and tension tests and UCS/UTS reaches its maximum and becomes independent of ϖ . On the other hand, for small ϖ ($\varpi = 0.33$), all the micro-cracks fail in shear ($\eta_{sc} = \eta_{st} = 100\%$) and UCS/UTS reaches its minimum. Though no additional simulations are conducted for $\varpi < 0.33$ as this is not the range of interest to us, we could expect that since there will be only shear micro-cracks at $\varpi = 0.33$, UCS/UTS is to remain constant at its minimum as shown in Huang and Detournay [12] for an elasto-perfectly brittle point contact model.

Additional insights into the relationships between the UCS/UTS and ϖ can be gained by examining the failure mechanisms at both the macro- and microscale. The macroscale failure mechanisms as reflected by the distribution of the micro-cracks from the uniaxial tests at 80% of the post-peak loading level are shown in Figs. 8 and 9 for $\chi = 6.67$ and $\varpi = 0.33$ and 3.33. Blue color denotes tensile micro-cracks and green for shear. Compared with the Berea sandstone model ($\varpi = 21.33$) in Fig. 4, the overall macroscale failure patterns in form of shear localization and tensile fracturing do not seem to be strongly affected by ϖ . However, the failure planes in direct tension become

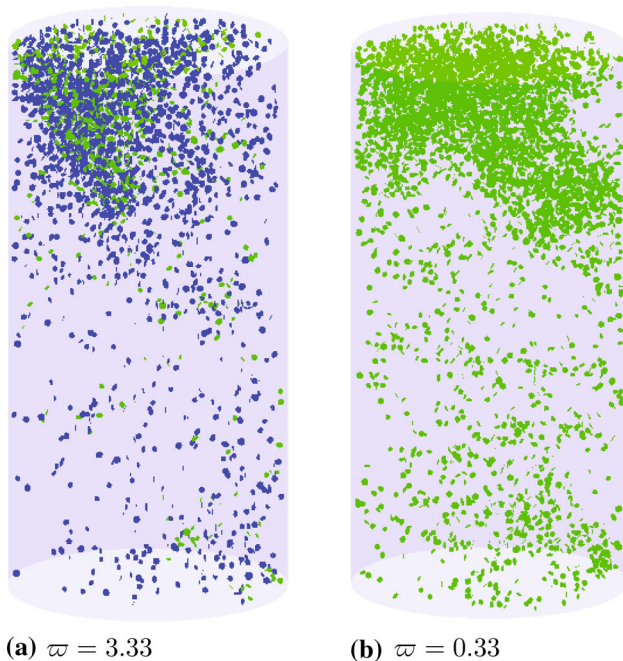


Fig. 8 Distributions of the micro-cracks from the uniaxial compression tests with $\chi = 6.67$; blue for tensile micro-cracks and green for shear (color figure online)

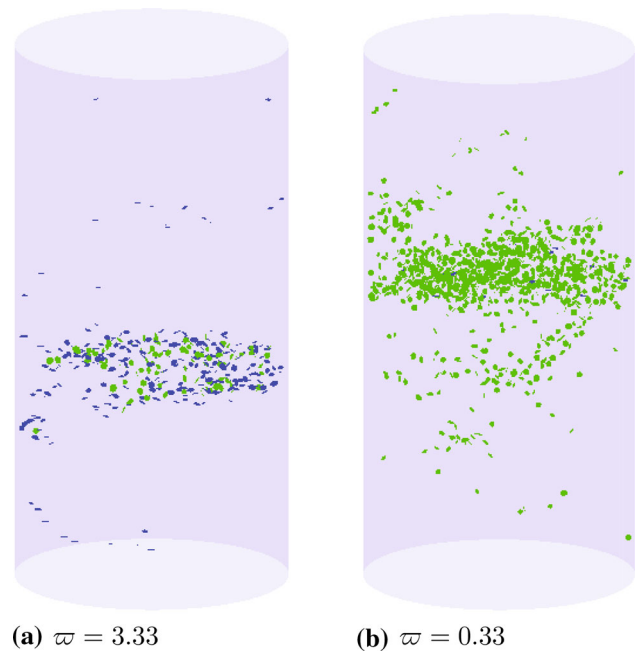


Fig. 9 Distributions of the micro-cracks from the direct tension tests with $\chi = 6.67$; blue for tensile micro-cracks and green for shear (color figure online)

notably more tortuous when ϖ decreases. At $\varpi = 0.33$, coalescence of the micro-cracks seems to form a non-planar feature in a spiral shape, an indication of hybrid tension and shear failure at the macroscale. Furthermore, as shown in Fig. 10, orientation of the micro-cracks, as measured by the angle between the normal to a micro-crack plane and a horizontal plane, is primarily subhorizontal at $\varpi = 3.33$, namely nearly perpendicular to the loading direction. Meanwhile, at $\varpi = 0.33$, orientation of the micro-cracks are mainly subvertical, i.e., nearly parallel to the loading direction. These evidences suggest that as far as the macroscale failure mechanisms are concerned, the DEM model becomes less brittle rock-like at $\varpi = 0.33$.

5 Effect of the softening coefficient

Effect of the softening coefficient χ is examined with four sets of simulations where the mean shear bond strength for the first three is $\bar{\tau}_c = 50, 150, 300$ MPa, i.e., $\varpi = 3.33, 10, 20$. In each set, χ varies from 0 to 100. The fourth set, denoted in the plots as $\varpi \gg 20$, is the limiting case. The value of $\bar{\tau}_c$ is chosen to ensure that only tensile micro-cracks occur and the results no longer change with any further increase in ϖ .

Variation of the uniaxial compressive strength with χ is shown in Fig. 11a. UCS increases with χ and reaches horizontal asymptotes as χ becomes large for $\varpi = 3.33$ and 10. Indeed, UCS remains constant when $\chi \gtrsim 20$ and

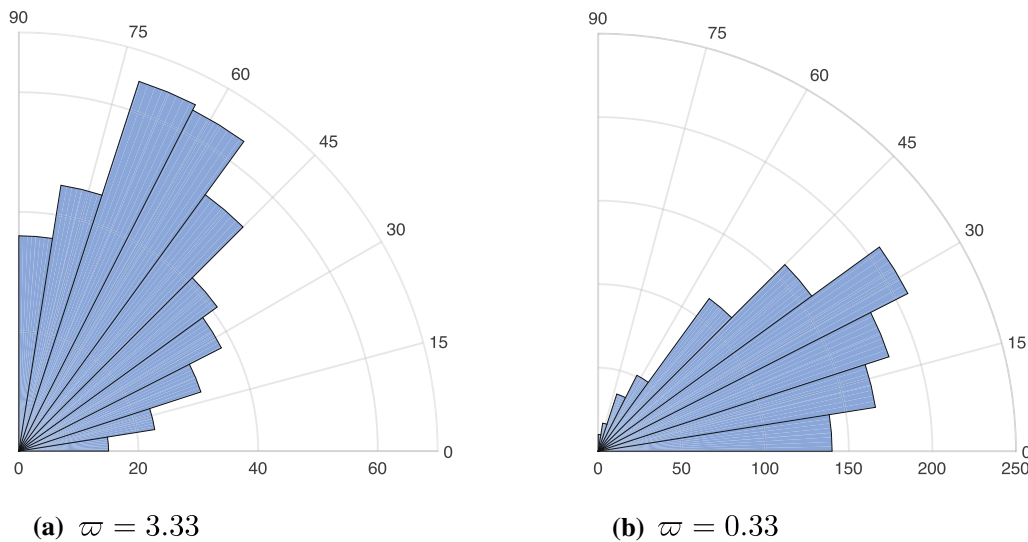


Fig. 10 Histograms for the orientation of the micro-cracks as measured by the angle between the normal to a micro-crack plane and a horizontal plane; direct tension tests with $\chi = 6.67$; **a** $\omega = 3.33$ and **b** $\omega = 0.33$

$\varpi = 3.33$. For the case of $\varpi \gg 20$, UCS increases nearly proportionally with χ and the curve serves as an envelope that bounds the other three cases. In all the cases, UCS is not affected by ϖ when $\chi \lesssim 1$.

Similar trends are also observed for the tensile strength, see Fig. 11b. It should be noted that for a given χ , UTS no longer increases when $\varpi \geq 10$. Results from the cases with $\varpi = 20$ and $\varpi \gg 20$ are identical to those with $\omega = 10$ and are therefore not plotted. It can be seen that UTS is independent of ϖ when $\chi \lesssim 20$.

The overall trends in the strength variations with χ can be explained by the microscale failure mechanisms. When the displacement softening law is active ($\chi \gtrsim 0.286$), the microscale failure mechanisms evolve from tension-governed to shear-governed as χ increases, see Fig. 12. $\chi \lesssim 1$ for UCS and $\chi \lesssim 20$ for UTS in these simulations show they are governed by normal bond failure only. Note that for the tensile tests with $\varpi = 3.33$, though Fig. 12 shows $\eta_{st} > 0$ when $5 \lesssim \chi \lesssim 20$, most of the shear micro-cracks occur after the peak; there are only tensile micro-cracks at the peak of these tests. Uniaxial strengths in these cases are therefore primarily affected by both the bond strength $\bar{\sigma}_c$ and the nominal energy loss density \bar{U}_b associated with one bond breakage. With $\bar{\sigma}_c$ being fixed in this series of simulations, \bar{U}_b increases with χ as shown in Eq. 4. Consequently, the uniaxial strengths increase with χ , but are independent of ϖ . The near-linear trend in the UCS when shear bond failure is neglected ($\varpi \gg 20$) suggests that $UCS \sim N\bar{U}_b$ where N is the total number of micro-cracks at the peak stress.

Meanwhile, when both shear and normal bond failures are involved, the nominal energy loss density \bar{U}_b can be revised according to,

$$\bar{U}_b = (1 - \eta_s)(1 + \chi) \frac{\bar{\sigma}_c^2}{E_c} + \eta_s \frac{\bar{\tau}_c^2}{E_c} \tag{6}$$

where $\eta_s = \eta_{sc}$ for uniaxial compression and $\eta_s = \eta_{st}$ for direct tension at the peak stress level. Since η_s (either η_{sc} or η_{st}) increases with χ , the contribution from the first term is expected to gradually diminish as η_s approaches unity and \bar{U}_b becomes constant, $\bar{U}_b = \bar{\tau}_c^2/E_c$. This explains why the rates of strength increase decrease with χ in Fig. 11a, b and at $\varpi = 3.33$ and 10, UCS becomes constant when χ is large as the failure mechanism now involves predominantly shear bond breakage, see Fig. 12.

Variation of the strength ratio UCS/UTS with χ is shown in Fig. 13. In the limiting case ($\varpi \gg 20$), UCS/UTS increases monotonically with χ . However, at $\varpi = 3.33$ and 10, dependence of UCS/UTS on χ is nonmonotonic, since the rates of strength increase with respect to χ are different in uniaxial compression and direct tension. Denote χ_* as the critical value that yields the peak UCS/UTS. The peak values are $UCS/UTS = 10.64$ at $\chi_* \simeq 5$ for $\varpi = 3.33$ and $UCS/UTS = 18.63$ at $\chi_* \simeq 20$ for $\varpi = 10$. Indeed, χ_* is in fact the threshold that marks the transition from $\eta_{st} = 0$ to $\eta_{st} > 0$ if χ increases, see Fig. 12 and Table 3. In other words, if $\chi > \chi_*$, shear bond failures appear in direct tension and UCS/UTS starts to observe a descending trend with χ . Since the shear micro-cracks in direct tension are less likely to occur at a larger ϖ , χ_* at $\varpi = 10$ is larger than that from $\varpi = 3.33$.

When $\varpi = 20$, though shear bond failures occur in uniaxial compression, the microscale failures in direct tension are all tension-governed for $\chi \leq 100$. It is thus expected that $\chi_* > 100$. Nevertheless, as χ increases from 50 to 100, UCS/UTS increases only slightly from 23.01 to

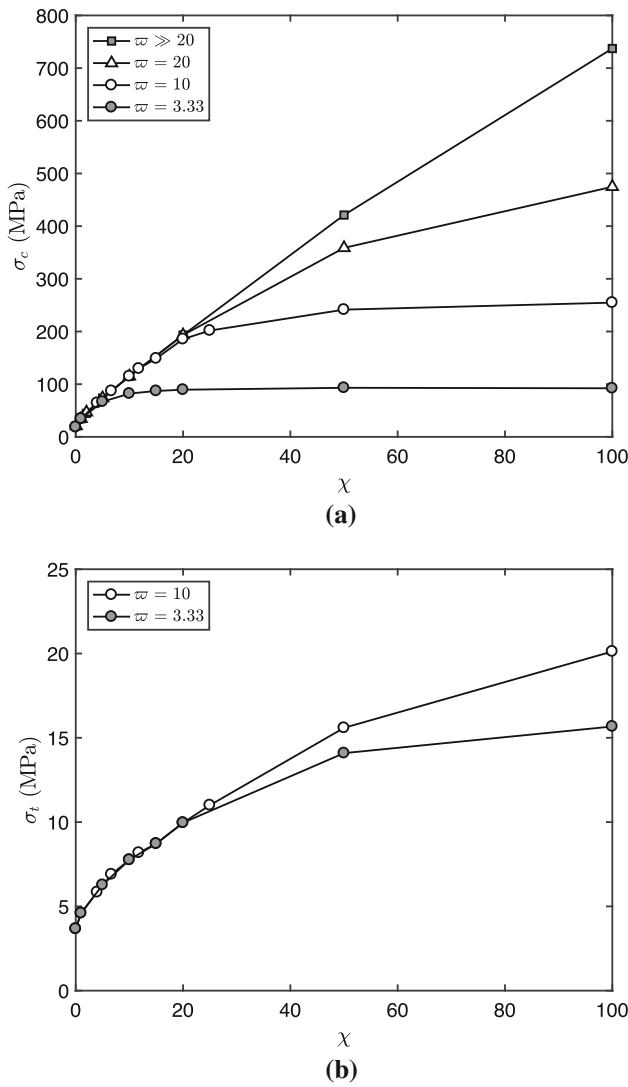


Fig. 11 Variations of the uniaxial compressive strength (a) and tensile strength (b) with χ

23.59. It is also noted that the curve for a given ϖ departs from this envelope when η_{sc} at the peak becomes non-zero, namely, when shear bond failure occurs in the compression test. The departure occurs at about $\chi = 15$ for $\varpi = 10$ and $\chi = 20$ for $\varpi = 20$.

Within the range of χ explored in this study ($0 \leq \chi \leq 100$), we may consider $\varpi \simeq 20$ as a critical case. Dependence of UCS/UTS on χ is nonmonotonic if $\varpi < 20$, but is monotonically increasing if $\varpi > 20$.

6 Discussions

If the shear bond failure is neglected, there are only two primary microscale bond strength parameters, i.e., the normal bond strength $\bar{\sigma}_c$ and the softening coefficient χ . Given a realistic set of uniaxial strengths, we can determine

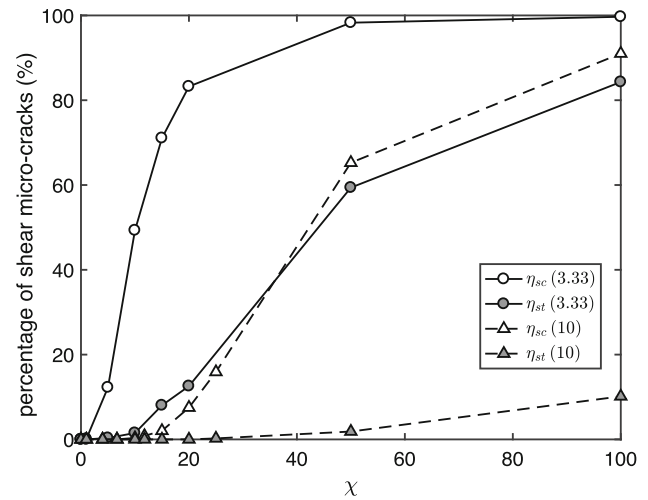


Fig. 12 Variation of the percentage of shear micro-cracks with χ at 80% of the post-peak loading level; $\varpi = 3.33$ and 10

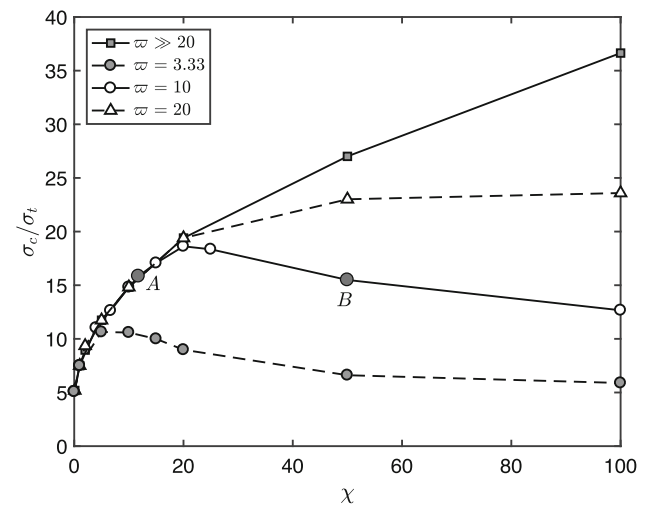


Fig. 13 Variations of the strength ratio UCS/UTS with the softening coefficient χ

the softening coefficient χ based on UCS/UTS from the limiting case ($\varpi \gg 20$) in Fig. 13. After that, we can determine the normal bond strength $\bar{\sigma}_c$ as it is proportional UTS (or UCS) when all other parameters remain constant.

However, if the shear bond strength $\bar{\tau}_c$ is effective, there are now three bond strength parameters, $\bar{\tau}_c$, $\bar{\sigma}_c$ and χ (or $\bar{\sigma}_c$, ϖ , χ), for the displacement-softening contact model. The choice of the microscale parameters becomes nonunique if only the uniaxial strengths are used for calibrating the material strength characteristics.

Results from the above simulations indicate that UCS/UTS depends on both the bond strength ratio ϖ and the softening coefficient χ , but the correspondence between UCS/UTS and the combination of ϖ and χ is nonunique. For example, for cases marked A and B in Fig. 13, though their strength ratios are about the same, χ is not; $\chi = 11.76$

Table 3 Strength ratio and the percentage of shear micro-cracks from 80% of the post-peak loading level with $\varpi = 10$

χ	UCS (MPa)	UTS (MPa)	UCS/UTS	η_{sc}	η_{st}
0.001	18.66	3.67	5.08	0	0
1	34.51	4.60	7.50	0	0
4	64.39	5.84	11.03	0	0
6.67	87.16	6.90	12.63	0.02	0
10	114.99	7.76	14.82	0.33	0
11.76 (A)	129.58	8.18	15.84	0.83	0
15	148.82	8.72	17.07	3	0
20	185.52	9.96	18.63	7.50	0
25	201.81	11.00	18.35	15.90	0.24
50 (B)	241.50	15.59	15.49	65.26	1.86
100	254.80	20.12	12.66	91.00	10.15

$\chi \approx 20$ is the threshold that marks the transition from $\eta_{st} = 0$ to $\eta_{st} > 0$

for case A and $\chi = 50$ for case B. In case A, $\sigma_c = 129.58$ MPa and $\sigma_t = 8.18$ MPa; and in case B, $\sigma_c = 241.5$ MPa and $\sigma_t = 15.59$ MPa. The strengths in case B are about 1.9 times of those in case A. Note that the magnitude of the strengths can be scaled by adjusting the normal bond strength $\bar{\sigma}_c$ while keeping ϖ and χ constant and is therefore not the main concern here.

One main difference between these two cases lies in the microscale failure mechanisms. In case A, the micro-cracks are mostly in tension, $\eta_{sc} = 0.83\%$ and $\eta_{st} = 0\%$ at 80% of the post-peak loading level; the ratios between the number of shear vs. tensile micro-cracks are 49:5837 and 0:458, respectively. Meanwhile, in case B, the shear micro-crack percentage increases to $\eta_{sc} = 65.26\%$ in uniaxial compression and $\eta_{st} = 1.8\%$ in direct tension; the ratios of the number of shear vs. tensile micro-cracks change to 1313:699 and 8:423. While the total numbers of the micro-cracks are comparable between the two cases in direct tension, the total number in case A is nearly three times of that in case B in uniaxial compression. The overall macroscale failure mechanisms are still comparable between the two cases, see Figs. 14 and 15.

Another difference between the two cases is in the shape of the stress–strain curves in direct tension, see Fig. 16. In uniaxial compression, the shapes of the two stress–strain curves are nearly identical. Nevertheless, in direct tension, the stress–strain curve from case B agrees with that from case A only when the strain is relatively small. Due to the relatively large χ , case B observes substantial strain hardening in direct tension. Since we are not attempting to calibrate the parameters for a specific material, we will reserve our judgment on whether such a shape is realistic or not. Stress–strain curves from direct tension tests are hard to find in the literature. Based on very limited data set [18], if we are modeling quasi-brittle materials such as rocks and

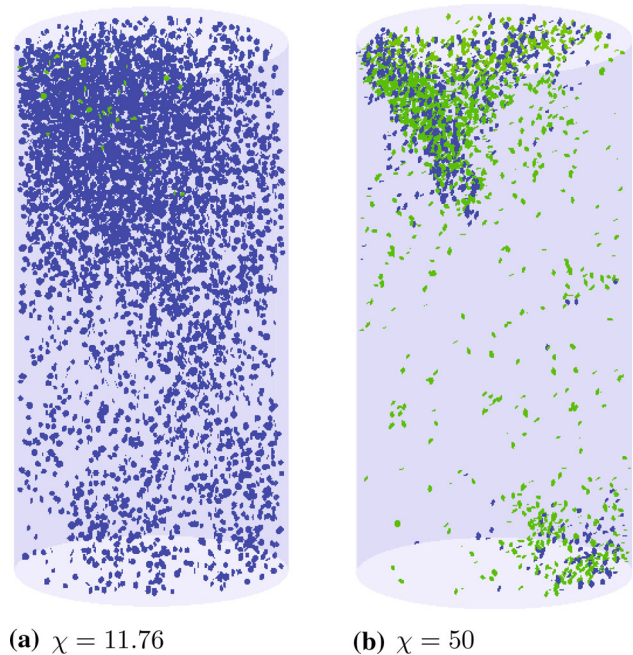


Fig. 14 Distribution of micro-cracks from uniaxial compression from cases A (a) and B (b); blue for tensile micro-cracks and green for shear (color figure online)

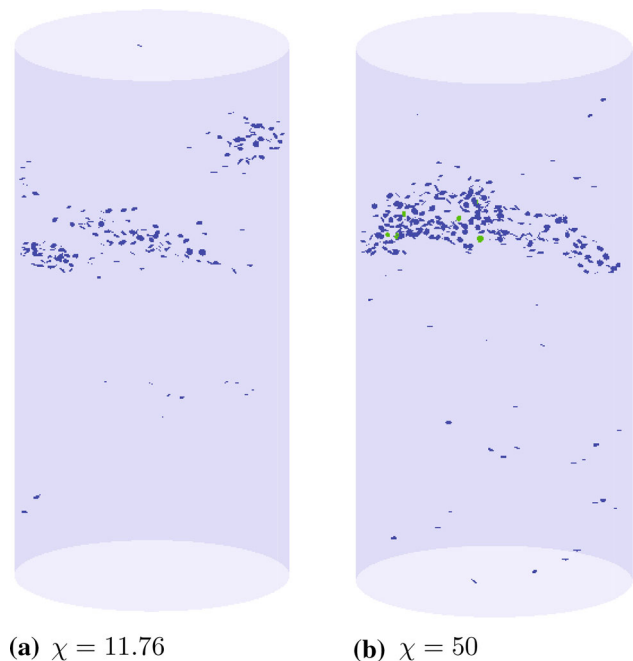


Fig. 15 Distribution of micro-cracks from direct tension from cases A (a) and B (b); blue for tensile micro-cracks and green for shear (color figure online)

concretes, the axial strain magnitude at the peak tensile stress in case B appears to be rather excessive. Parameters for case A are more reasonable choices.

Comparison between these two cases shows that to uniquely determine both ϖ and χ , UCS/UTS alone is

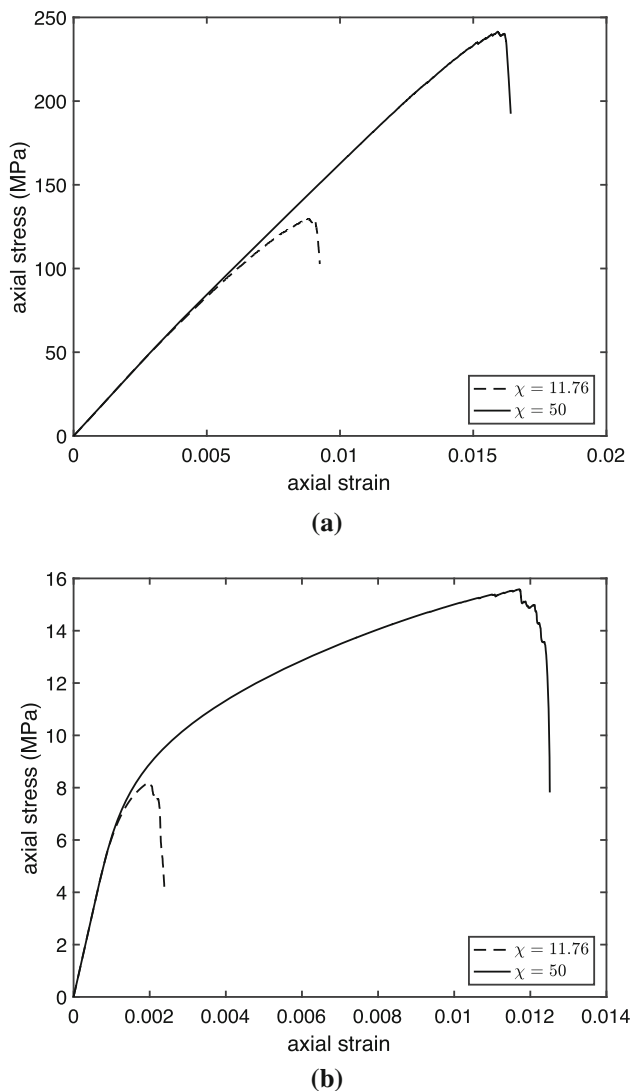


Fig. 16 Stress–strain curves from cases A and B; **(a)** uniaxial compression and **(b)** direct tension

insufficient. The main reason that this displacement-softening contact model could increase the UCS/UTS to realistic values is due to the fact that displacement softening at the contact level results in progressive failure and consequently strain hardening in both the uniaxial compression and direct tension test. Therefore, the stress–strain curves, in particular, the axial strains when the peak stresses are reached in the uniaxial tests could be an important piece of information for calibration against a specific rock. Moreover, microscale failure characteristics such as the source mechanisms associated with the micro-crack events could also be the additional aspects for consideration. It is however important to make the distinction among the macroscale failure mechanisms, microscale bond breakage and the acoustic emission source mechanisms since both the macroscale failure mechanisms and the AE source

mechanisms describe the deformation modes while the microscale breakages are associated with bond strengths.

An alternative approach is to include the full failure envelope in the parameter calibration. Though in this work, only the full failure envelope for the Berea sandstone model is shown, we could still deduce the effects of ϖ and χ on the shape of the failure envelope by comparing the result in Fig. 5 with the linear failure envelope obtained from the perfectly brittle contact model ($\chi = 0$) in Huang et al. [13]. We may approximate the failure envelope of the numerical sample by a Mohr-Coulomb criterion with a tension cutoff. Denote ω as the ratio between the limiting confining stress where the tension cutoff ends and the uniaxial tensile strength. The shape of the failure envelope can then be characterized by ω and the internal friction angle ϕ . When there is no shear bond failure ($\varpi \gg 20$), the friction angles from the Berea sandstone model with $\chi = 6.67$ and the model with $\chi = 0$ in Huang et al. [13] are comparable about $35^\circ \sim 36^\circ$. Therefore, the effect χ is to increase ω so that the tension cutoff becomes more prominent. Meanwhile, as shown in Figs. 6 and 11, between the two series of $\varpi = 3.33$ and 10, the tensile strength is not affected by ϖ when χ ranges from 0 to 20, but the compressive strength and UCS/UTS increases with ϖ . This means increase in the percentage of shear bond failure causes the friction angle ϕ as well as ratio ω to decrease.

In general, we are often limited by the availability of data, especially, data from direct tension and triaxial extension tests. Assuming shear bond failure could be neglected is therefore a reasonable starting point as a friction angle about $35^\circ \sim 36^\circ$ is typical for realistic rocks. The softening coefficient χ can then be determined based on the strength ratio from the bounding curve in Fig. 13. For modeling rocks with a relatively low friction, introducing shear bond failure is likely necessary. However, it should be noted that for rocks with a rather high friction angle, e.g., the Lac du Bonnet granite, though this contact model is able to reproduce a realistic strength ratio, the friction angle from the 3D numerical model is not as high [17]. The current model will need to be improved to consider factors such as grain angularity and intragranular failure which are critical in the failure behaviors of rocks such as granite.

7 Conclusions

Displacement softening as an ingredient to increase the compressive over tensile strength ratio to realistic values for DEM modeling is investigated in this study. In particular, we focus on the case where the force–displacement law for the normal bond component has a softening path

and the shear bond component remains elasto-perfectly brittle. Effects of both the softening coefficient χ and the bond strength ratio ϖ on the compressive over tensile strength ratio, the macro- and microscale failure mechanisms are analyzed. The main findings can be summarized as follows:

- Realistic compressive over tensile strength ratio can be effectively produced by the displacement-softening contact model. Both the uniaxial compressive strength and the tensile strength can be calibrated simultaneously.
- For a given softening coefficient χ , UCS/UTS decreases if shear bond failure becomes involved. UCS/UTS is the smallest if the micro-cracks all fail in shear in both uniaxial compression and direct tension test. UCS/UTS increases with shear over normal bond strength ratio ϖ only when both shear and tensile micro-cracks are present. When ϖ is larger than a threshold value, shear micro-cracks are no longer present and UCS/UTS reaches its maximum.
- For $0 \leq \chi \leq 100$, given a bond strength ratio ϖ , dependence of UCS/UTS on χ is nonmonotonic if $\varpi < 20$. The maximum value of UCS/UTS is obtained at a critical value of χ_* . At $\chi > \chi_*$, shear micro-cracks start to appear in direct tension. However, for $\varpi > 20$, UCS/UTS increases with χ monotonically. UCS/UTS becomes independent of ϖ when ϖ becomes large.
- If shear bond failure occurs at the microscale, the three primary bond strength parameters, $\bar{\sigma}_c$, ϖ , and χ , can no longer be uniquely determined based on the uniaxial strengths alone. For practical purposes, as we are usually limited by the availability of data, assuming the role of ϖ could be neglected is a reasonable starting point. The softening coefficient χ can then be determined based on the bounding curve in Fig. 13.
- Future work is needed to examine additional aspects of the failure characteristics at both the macro- and microscale in order to establish a reliable material property calibration procedure. In addition, it could also be worthwhile to include displacement softening in the shear bond component, which of course will make the calibration procedure even more complicated, but could potentially give the flexibility to model the material behaviors with higher fidelity.

References

1. Bobich JK (2005) Experimental analysis of the extension to shear fracture transition in Berea sandstone. Master's Thesis, Texas A&M University
2. Brace WF (1964) State of stress in the earth's crust. In: Judd WR (ed) Brittle fracture of rocks. Elsevier, New York, pp 110–178
3. Cho N, Martin CD, Segol DC (2007) A clumped particle model for rock. *Int J Rock Mech Min Sci* 44(7):997–1010
4. Cundall PA, Strack ODL (1979) A discrete numerical model for granular assemblies. *Geotechnique* 29(1):47–65
5. Fairhurst C (1964) On the validity of the Brazilian test for brittle materials. *Int J Rock Mech Min Sci Geomech Abstr* 1(4):535–546
6. Fowell RJ (1993) The mechanics of rock cutting. In: Hudson JA (ed) *Comprehensive rock engineering*, vol 4. Pergamon Press Ltd., Oxford, pp 155–176
7. Haimson B (2007) Micromechanisms of borehole instability leading to breakouts in rocks. *Int J Rock Mech Min Sci* 44(2):157–173
8. Hampton J, Gutierrez M, Matzar L, Hu D, Frash L (2018) Acoustic emission characterization of microcracking in laboratory-scale hydraulic fracturing tests. *J Rock Mech Geotech Eng* 10(5):805–817
9. Hoek E, Bieniawski ZT (1965) Brittle fracture propagation in rock under compression. *Int J Fract Mech* 1(3):137–155
10. Hoek E, Martin CD (2014) Fracture initiation and propagation in intact rock—a review. *J Rock Mech Geotech Eng* 6(4):287–300
11. Huang H (1999) Discrete element modeling of tool-rock interaction. Ph.D. Thesis, University of Minnesota
12. Huang H, Detournay E (2008) Intrinsic length scales in tool-rock interaction. *Int J Geomech* 8(1):39–44
13. Huang H, Lecampion B, Detournay E (2013) Discrete element modeling of tool-rock interaction I: rock cutting. *Int J Numer Anal Methods Geomech* 37(13):1913–1929
14. Itasca Consulting Group, Inc (2015) PFC3D—particle flow code in 3-dimensions, Ver. 5.0. Minneapolis, MN
15. Ma Y, Huang H (2017) Tensile strength calibration in DEM modeling. In: 51st US rock mechanics/geomechanics symposium. American Rock Mechanics Association
16. Ma Y, Huang H (2018a) DEM analysis of failure mechanisms in the intact Brazilian test. *Int J Rock Mech Min Sci* 102:109–119
17. Ma Y, Huang H (2018b) A displacement-softening contact model for discrete element modeling of quasi-brittle materials. *Int J Rock Mech Min Sci* 104:9–19
18. Okubo S, Fukui K (1996) Complete stress–strain curves for various rock types in uniaxial tension. *Int J Rock Mech Min Sci* 33(6):549–556
19. Pierce M, Cundall P, Potyondy DO, Mas Ivars D (2007) A synthetic rock mass model for jointed rock. In: Proceedings of 1st Canada-US rock mechanics symposium, rock mechanics: meeting society's challenges and demands, Vancouver, vol 1, pp 341–349
20. Potyondy DO (2012) A flat-jointed bonded-particle material for hard rock. In: Proceedings of 46th US rock mechanics/geomechanics symposium. American Rock Mechanics Association, Chicago, USA
21. Potyondy DO (2018) A flat-jointed bonded-particle material for rock. In: Proceedings of 52th US rock mechanics/geomechanics symposium. American Rock Mechanics Association, Seattle, WA
22. Potyondy DO, Cundall PA (2004) A bonded-particle model for rock. *Int J Rock Mech Min Sci* 41(8):1329–1364
23. Qu J, Cherkaoui M (2007) Fundamentals of micromechanics of solids. Wiley, New York
24. Ramsey J, Chester F (2004) Hybrid fracture and the transition from extension fracture to shear fracture. *Nature* 428(6978):63–66
25. Scholtès L, Donzé FV (2013) A DEM model for soft and hard rocks: role of grain interlocking on strength. *J Mech Phys Solids* 61:352–369

26. Stead D, Eberhardt E, Coggan JS (2006) Developments in the characterization of complex rock slope deformation and failure using numerical modelling techniques. *Eng Geol* 83(1–3):217–235
27. Tarokh A, Fakhimi A (2014) Discrete element simulation of the effect of particle size on the size of fracture process zone in quasi-brittle materials. *Comput Geotech* 62:51–60
28. Teufel LW, Clark JA (1981) Hydraulic-fracture propagation in layered rock: experimental studies of fracture containment. Technical report, Sandia National Labs., Albuquerque, NM (USA)
29. Wong TF, David C, Zhu W (1997) The transition from brittle faulting to cataclastic flow in porous sandstones: mechanical deformation. *J Geophys Res Solid Earth* 102(B2):3009–3025
30. Zietlow WK, Labuz JF (1998) Measurement of the intrinsic process zone in rock using acoustic emission. *Int J Rock Mech Min Sci* 35(3):291–299

Publisher's Note Springer Nature remains neutral with regard to jurisdictional claims in published maps and institutional affiliations.